Hindawi
Advances in Materials Science and Engineering
Volume 2018, Article ID 4873571, 11 pages
https://doi.org/10.1155/2018/4873571

Research Article

Nanoindentation Hardness Distribution and Strain Field and Fracture Evolution in Dissimilar Friction Stir-Welded AA 6061-AA 5A06 Aluminum Alloy Joints

Guangjian Peng,[1,2] Yi Ma,[1] Jiangjiang Hu,[1] Weifeng Jiang,[1] Yong Huan,[3] Zhitong Chen,[4] and Taihua Zhang[1]

[1]*College of Mechanical Engineering, Zhejiang University of Technology, Hangzhou 310014, China*
[2]*Department of Mechanical Engineering, Johns Hopkins University, Baltimore, MD 21218, USA*
[3]*State Key Laboratory of Nonlinear Mechanics (LNM), Institute of Mechanics, Chinese Academy of Sciences, Beijing 100190, China*
[4]*Department of Mechanical and Aerospace Engineering, The George Washington University, Washington, DC 20052, USA*

Correspondence should be addressed to Zhitong Chen; zhitongchen@gwu.edu and Taihua Zhang; zhangth@zjut.edu.cn

Received 1 August 2018; Accepted 26 August 2018; Published 11 October 2018

Academic Editor: Stanislaw Dymek

Aluminum alloy AA 6061-T651 and 5A06-H112 rolled plates were successfully welded by friction stir welding (FSW) at three rotation speeds of 600, 900, and 1200 rpm with two transverse speeds of 100 and 150 mm/min. Mechanical properties and strain field evolution of FSW AA 6061-AA 5A06 were characterized by the uniaxial tension and digital image correlation (DIC) tests. Furthermore, the hardness distribution map of whole cross section was obtained via the nanoindentation method with 700 indents. Both DIC and nanoindentation results reveal that the heat-affected zone (HAZ) of AA 6061 alloy is the softest area in the weldment, and the fracture happens in this region. The microstructure evolution characterized by electron-backscatter diffraction (EBSD) indicates that the continuous dynamic recrystallization is the primary grain structure evolution in the stirring zone, and the grain refinement helps improve the mechanical properties. Analyses of the micro- and macrofeatures of the fracture surfaces via scanning electron microscopy (SEM) and optical microscope suggest that the increasing of heat input could enlarge the size of HAZ and reduce the slant angle of HAZ and thus lead the fracture angle to decrease and cause the dimples change from inclined ones to normal ones.

1. Introduction

In the past decades, aluminum alloys have been used as an alternative to steel due to their high strength-to-weight ratio, superior formability and machinability, and excellent corrosion resistance [1–3]. However, conventional fusion welding methods are not suitable for aluminum alloys, particularly for dissimilar aluminum alloys. It has been clearly confirmed that conventional fusion welding methods have a series of severe issues, including the formation of secondary brittle phases, porosity and cracking during solidification, large welding deformation, and high residual stresses [4–6]. In order to solve problems of conventional fusion welding, it is of great importance to introduce a low-cost, environmentally friendly manufacturing process, with high productivity. Friction stir welding (FSW) is a solid-state welding method, which is invented by The Welding Institute (TWI) and has been demonstrated particularly suitable for joining aluminum alloys [7, 8].

During the FSW, a rotating tool with pin and shoulder is inserted into the workpiece and then moves along the welding direction. Frictional heat causes the alloys to soften and allows the tool to traverse along the joint line. There is no melting in the FSW process, which is beneficial for the FSW to avoid the welding issues occurring in the conventional fusion welding mentioned earlier. Therefore, the FSW

should be considered as an effective and reliable process for the welding of aluminum alloys [7]. The FSW process generates three distinct microstructural zones: the nugget zone (NZ), the thermomechanically affected zone (TMAZ), and the heat-affected zone (HAZ) [9–11]. The NZ is the region that experiences dynamic recrystallization process because of the effect of strong mechanical stirring and high heat input, which generally consists of fine and equiaxed grains. The TMAZ adjacent to the NZ exhibits plastic deformation under the thermomechanical effects. The HAZ experiences only heating effect without any mechanical action. There have been a number of papers highlighting the microstructural and mechanical changes from the parent material to the welding nugget zone [12–17]. The microstructure and mechanical properties depend on the relative plastic deformation and heat distribution during FSW process. Coarsening of strengthening precipitates and dissolution as well as the formation of wide precipitate-free zones have been found. The local nucleation, growth, and coarsening processes for strengthening precipitates are a function of temperature, which in turn is now a function of distance from the weld nugget [18–20]. Mechanical failure of the welds can occur in the NZ, HAZ, or TMAZ depending on the amount of heat input, which is controlled by welding parameters such as pin profile, tool rotation, and travel speeds [21–23]. In FSW, the process parameters exerted significant impact on the microstructural characteristics, mechanical properties, and residual stress distributions of welds; therefore, it is necessary to optimize the process parameters to improve the welding quality and decrease welding defects [24, 25].

Nonheat treatable 5A06 aluminum alloys (Al-Mg alloy) have a better anticorrosion performance and excellent mechanical properties, whereas heat treatable 6061 aluminum alloys (Al-Mg-Si alloy) are versatility in strength and toughness [26]. Combination of these aluminum alloys could improve their performance and broaden applications in aerospace, automotive, and marine. In this paper, AA 6061-T651 and AA 5A06-H112 were joined together via friction stir weld at different welding parameters. Digital image correlation (DIC) and uniaxial tension were employed to investigate the variations of mechanical properties including yield strength, ultimate tensile strength, strain field evolution, and fracture features. A large number of nanoindentation tests were also carried out to obtain the hardness distribution to reveal the softest region in the weldment [27, 28]. A comprehensive analysis of mechanical properties and microstructure in FSW AA 6061 and AA 5A06 was proposed. Although the FSW process is now well established in joining of Al-alloys in similar combinations, there is still a need to fully understand the joint characteristics in dissimilar FSWed Al-alloy joints.

2. Experiments

2.1. Materials and FSW. Friction stir welds were carried out on 5 mm-thick AA 6061-T651 and AA 5A06-H112 rolled plates whose chemical compositions are listed in Table 1. Both aluminum plates were cut into rectangular shape measuring 200 mm in length and 100 mm in width. A stir tool with a shoulder of 16 mm diameter and a conical probe of 4.6 mm length was used. The conical probe has three grooves, and the specific dimensions are shown in Figure 1(b). The principal directions of FSW geometry were denoted as follows: welding direction (WD), rolling direction (RD), and normal direction (ND). Single-pass butt friction stir welds were performed perpendicular to the rolling direction of the plates by placing AA 6061 on the advancing side as shown in Figure 1(a). During the FSW process, the tool was put on a 2° tilt angle and 4.7 mm plunge depth. Three tool rotation speeds (RS) and two welding transverse speeds (TS) as listed in Table 2 were considered.

2.2. Uniaxial Tension and Digital Image Correlation Tests. Three tensile specimens were obtained from each welded plate according to ASTM E8M, as shown in Figure 1(c). For each specimen, 1 mm thickness of the top surface and 0.5 mm thickness of the bottom surface were machined away, to make the specimen flat with uniform cross section in the gauge. The uniaxial tensile tests were carried out in a material testing system MTS 810 with a constant extension speed of 1.5 mm/s. The yield strength and ultimate tensile strength were obtained, and the average value was used for analysis. During tensile tests, a two-dimensional digital image correlation (DIC) system was employed to monitor the stain field near the joint.

2.3. Nanoindentation Tests. Nanoindentation specimens with the length of 29 mm and thickness of 3 mm were cut from the joint area as shown in Figure 1(c). Then, the side surface of the specimen was polished to mirror finish via an automatic polishing machine with 0.3 μm alumina powder. An Agilent Nano Indenter G200 system with a modified Berkovich indenter was used to conduct nanoindentation tests. To quantitatively evaluate the distribution of indentation hardness in the joint area, an array that consists of 700 indents was carried out on the side surface of the specimen, with 400 μm space between very two indents. For each nanoindentation test, the indentation load was increased linearly to a maximum load of 120 mN in 30 seconds, then held for 10 seconds, and finally linearly decreased to zero in 30 seconds. During indentation tests, the thermal drift rate was within ±0.05 nm/s. The possible maximum thermal drift was ±3.5 nm for a test lasting 70 seconds, which was much smaller than the indentation depth (about 2 μm).

2.4. Microstructure Analysis. Microstructural characterization of the weld region was performed by electron-backscatter diffraction (EBSD). An SEM equipped with an EBSD system was used to conduct the high-resolution EBSD analysis. Scanning electron microscopy (SEM) was employed to analyze the microstructure of the fracture surface of tensile specimens. And energy dispersive spectroscopy (EDS) analysis was also performed to assess alloy elements of fracture surface.

Table 1: Chemical composition of AA 5A06, AA 6061, and the fracture surface of the welded specimen (wt.%).

	Si	Fe	Cu	Mn	Mg	Cr	Zn	Ti	Al
AA 5A06	0.30~0.40	≤0.40	0.05~0.10	0.50~0.80	5.80~6.80	—	0.10~0.20	0.02~0.10	Bal.
AA 6061	0.40~0.80	≤0.70	0.15~0.40	≤0.15	0.80~1.20	0.04~0.35	≤0.25	≤0.15	Bal.
Fracture surface	0.79	0.70	0.35	0.08	1.46	0.17	0.08	0.21	96.16

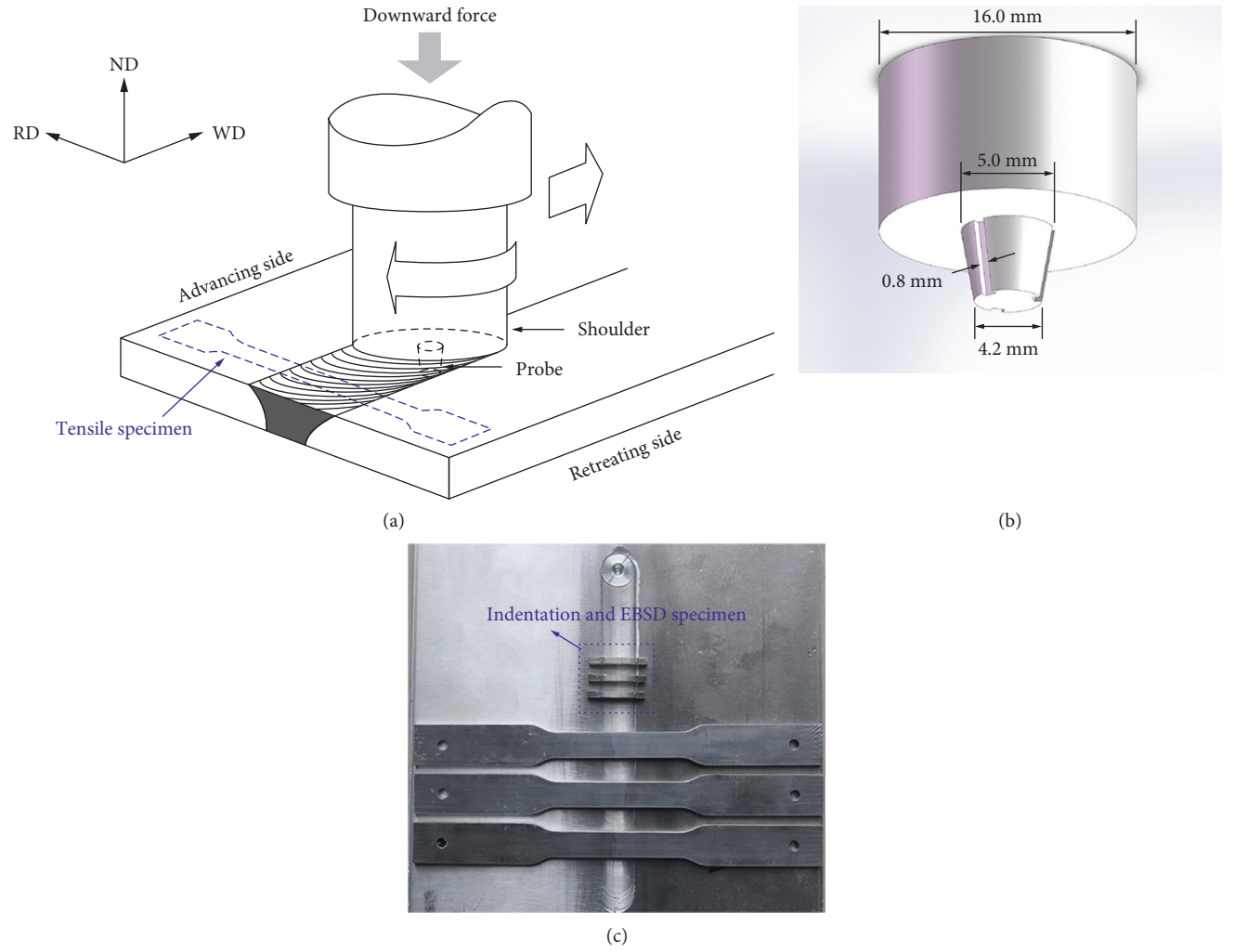

Figure 1: (a) Schematic drawing of the FSW joining process, (b) specific dimensions of the tool, and (c) the locations where tensile, indentation, and EBSD specimens were obtained.

Table 2: Investigated welding parameters in experimental scale-up processing.

Samples	RS (rpm)	TS (mm/min)	RS/TS (r/mm)
Sample 1	600	150	4
Sample 2	900	150	6
Sample 3	1200	150	8
Sample 4	600	100	6
Sample 5	900	100	9
Sample 6	1200	100	12

3. Results and Discussion

3.1. Tensile Properties. The representative engineering stress-strain curves of FSW joints and original AA 6061 and AA 5A06 are shown in Figure 2. For AA 6061 plates, the average yield strength is 236.17 MPa, the average ultimate tensile strength is 277.67 MPa, and the average elongation at break is 13.08%; for AA 5A06 plates, the average yield strength, ultimate tensile strength, and elongation at break are 125.78 MPa, 307.87 MPa, and 22.13%, respectively. It should be pointed out that the engineering stress-strain curves of FSW joints overlapping with the curve of AA 5A06 at the beginning is a coincidence (Figure 2). Comparison of the alloy elements as listed in Table 1 reveals that the yielding, necking, and fracture all occur at the AA 6061 side. This means the yield strength drops 50% to ~115 MPa and the ultimate tensile strength reduces from 277.67 MPa to ~190 MPa for AA 6061 in the FSW joints. Generally, the heat input introduced by FSW could affect the mechanical properties of joints a lot. For the present FSW joints, the

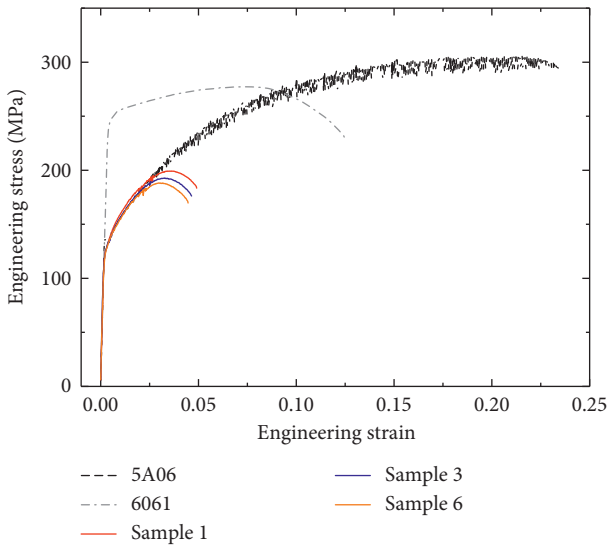

Figure 2: Engineering stress-strain curves of the FSW AA 6061-AA 5A06 specimens as compared to those of base metals AA 6061 and AA 5A06.

heat input definitely affects the mechanical properties of the AA 6061. As Peel et al. pointed out, this is mainly because the rolled AA 6061 stays in an extremely work hardened state and has a highly unstable microstructure, which will recrystallize readily under the elevated temperature generated during FSW [29]. The recrystallization will destroy the work hardened state and cause the mechanical properties to be weakened. It is commonly regarded that the higher R/T ratio (the ratio of rotational speed to transverse speed) leads to higher temperature and heat input [30–32]. Figure 3 shows both the yield strength and the ultimate tensile strength of FSW joints reduce slightly (within 10%) even while the R/T ratio increases from 4 r/mm to 12 r/mm. This means the increase of heat input does not affect the yield strength and ultimate tensile strength much. It could be inferred that the temperature generated by FSW at the R/T ratio of 4 is high enough to trigger the recrystallization of rolled AA 6061 and destroy the work hardened state.

3.2. Strain Field Evolution. The evolution of strain field near the joints was monitored by DIC during uniaxial tensile tests. Due to the limitation of space, the strain field evolution of Sample 1 is illustrated in Figure 4 as a representative one. Figure 4(a) shows that the strain distributes uniformly before yielding. With the extension of the specimen, yielding first occurs in the HAZ of the AA 6061 side as shown in Figure 4(b). It is clear from Figures 4(c)–4(e) that another weak area (red area) appears as the extension increases. The newly appeared weak area indicates the joint interface which could be clearly seen in Figure 5(a). Though the ratio of rotational speed to transverse speed increases from 4 r/mm to 12 r/mm, a joint interface exists in the NZ for all FSW samples. This means AA 6061 and AA 5A06 are difficult to merge to form "onion ring." In the current FSW samples, the HAZ of AA 6061 and the joint interface are two weak areas. During the tensile tests, there is a competition between the HAZ of AA 6061 and the joint interface. The evolution of strain field shown in Figures 4(e)–4(j) demonstrates that the joint interface won the competition and the HAZ of AA 6061 is the weakest area.

3.3. Cross Section and Nanoindentation Results. Figure 5(a) shows an optical micrograph of the cross section of FSW AA 6061-AA 5A06, after etching in Keller's reagent at 0°C for 15 seconds. Differences in the absolute shear strain rate between the advancing and the retreating sides of the weld result in an asymmetric shape. The advancing side of the weld is where the rotational velocity of the tool has the same direction as its travel velocity, whereas on the retreating side of the weld, the two velocity components having opposite directions. The NZ, TMAZ, HAZ, and based material (BM) were labelled in Figure 5(a). Generally, the order of average grain size for each zone is HAZ > TMZ > NZ [33]. The size and shape of grains in the extruded section are highly dependent on the extrusion ratio. The nanoindentation hardness distribution is shown in Figure 5(b), and it is evident that the lowest hardness locates in the HAZ of AA 6061. Since the yield strength being proportional to the hardness for metals, this could intuitively explain why the yielding first occurs in the HAZ of AA 6061 during tensile tests. It could be noted that the shape and orientation of the yielding band shown in Figure 4(b) agree well with that of the lowest hardness area as shown in Figure 5(b). Figure 6 shows the representative nanoindentation load-depth curves for different areas of the welds (the position of selected indents were marked in Figure 5(a)). It is clear from Figure 6(a) that the load-depth curves for BM, HAZ, and NZ of the AA 6061 side deviate from each other. Typically, a steeper load-depth curve indicates higher nanoindentation hardness. Thus, the hardness for each zone is BM > NZ > HAZ for the AA 6061 side. This demonstrates that the mechanical properties of AA 6061 were weakened after FSW. In Figure 6(b), the good superposition of the load-depth curves for different areas of the AA 5A06 side indicates that the change of mechanical properties for each zone is small after FSW. The hardness in NZ and TMAZ is slightly higher than that in BM (the reason is discussed in Section 3.4). It could be summarized from Figures 5(b) and 6 that the mechanical properties of AA 6061 are more sensitive to the heat input than those of AA 5A06.

3.4. Grain Structure of the Weld Region. The EBSD grain images in Figure 7 show that the grain size in the stirring zones is much smaller than that in the base materials. This can be related to the effect of dynamic recovery and recrystallization. Dynamic recovery and recrystallization are the main mechanisms for grain refinement during FSW [34, 35]. With increase of strain, dislocation is generated and a rapid multiplication of dislocation occurs. A progressive increase in dislocation density with increasing strain leads to three-dimensional arrays of low-angle grain boundaries transforming to high-angle grain boundaries

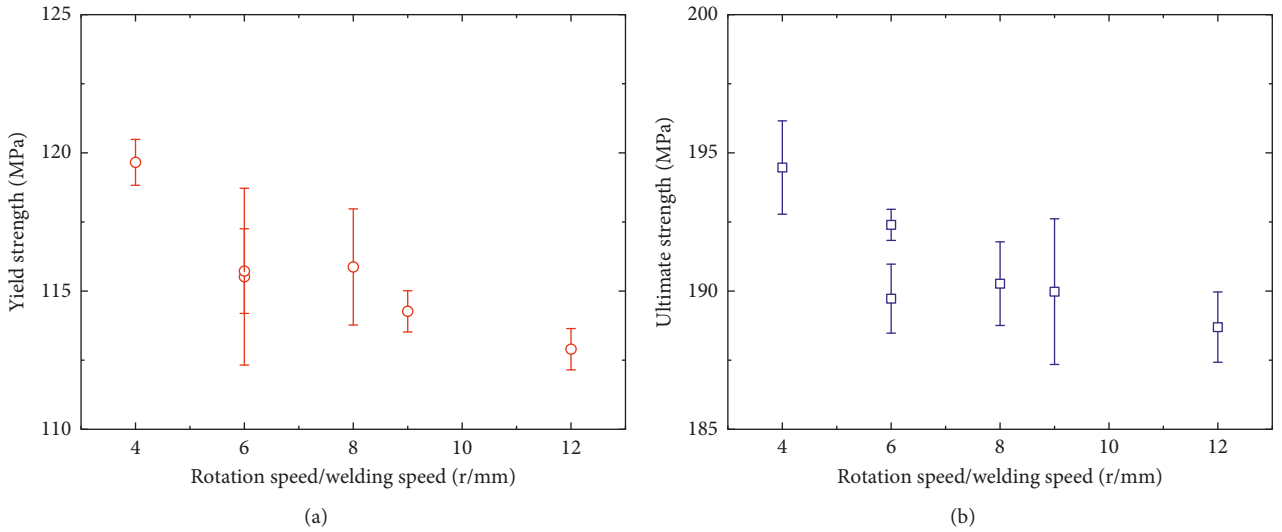

Figure 3: The variation of (a) yield strength and (b) ultimate tensile strength with the ratio of rotation speed to welding speed.

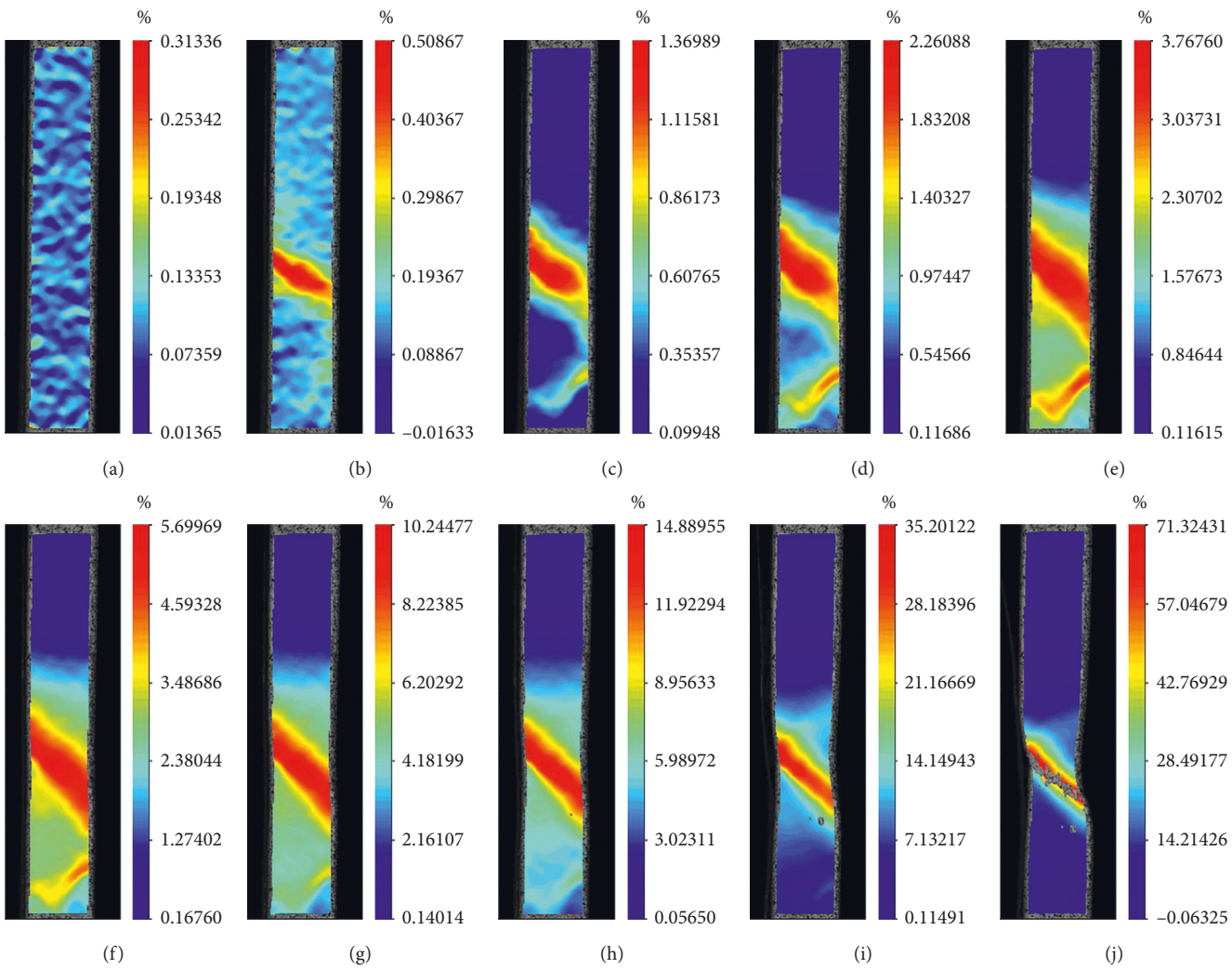

Figure 4: The strain field evolution of the weld region of Sample 1 monitored by DIC.

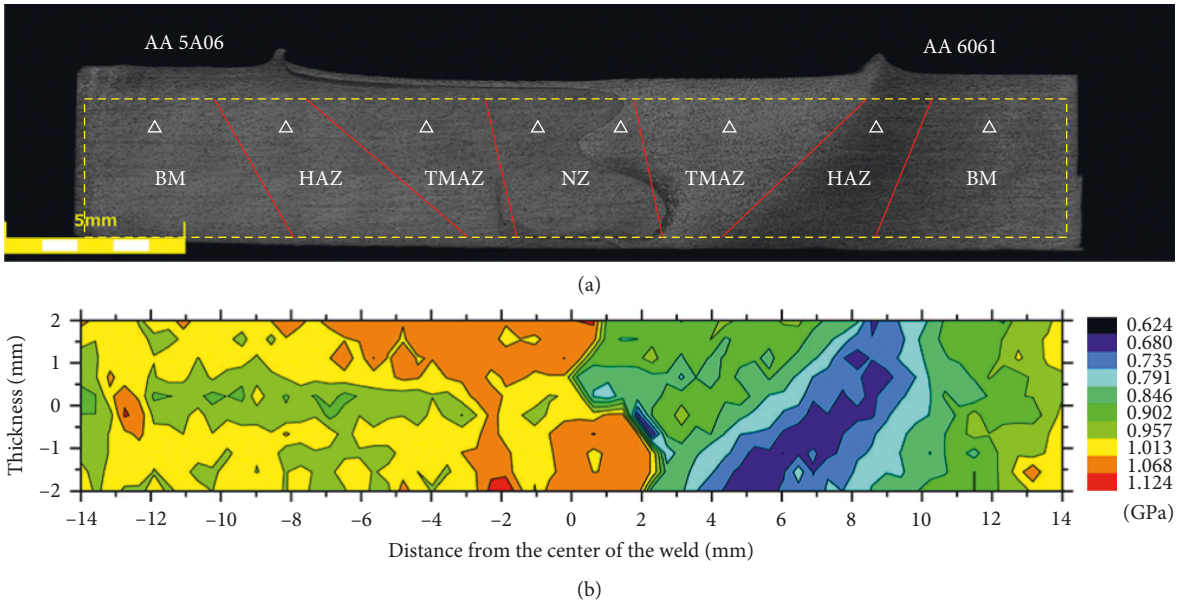

Figure 5: (a) The cross-sectional view of FSW AA 6061-AA 5A06, and (b) nanoindentation hardness distribution on the cross section.

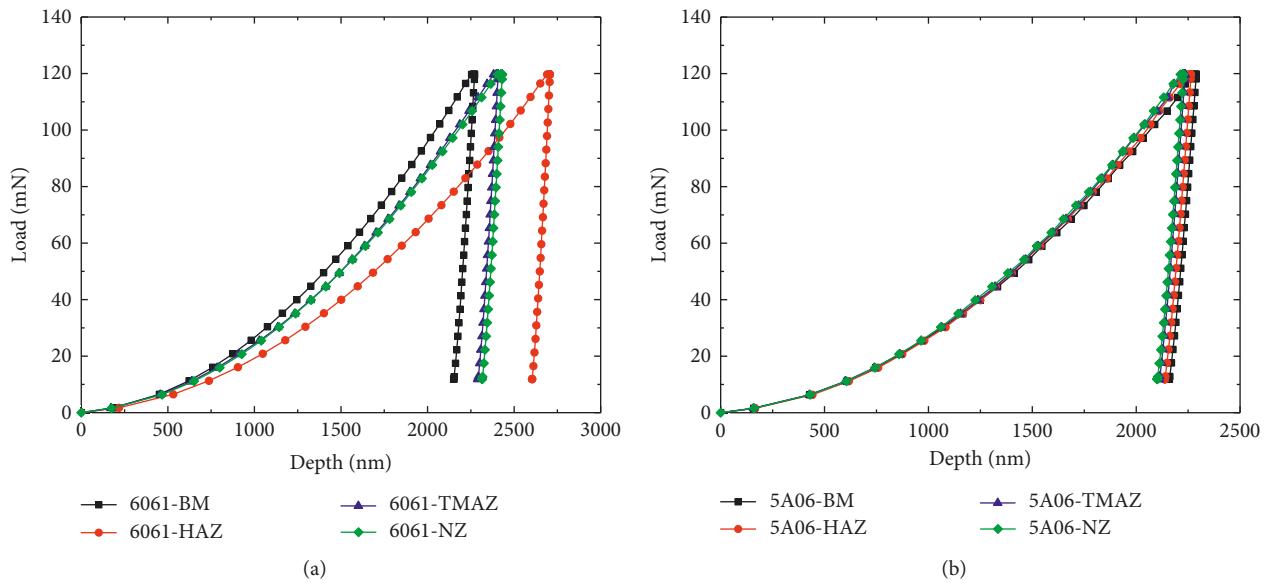

Figure 6: Typical nanoindentation load-depth curves for different areas of the FSW joint at (a) the AA 6061 side and (b) the 5A06 side.

during FSW. Individual segments of high-angle grain boundaries replace subgrains evolved at small strains, and grain size refinement occurs. Presence of vibration partially increases the temperature in the weld region, and additionally enhances the work hardening and leads to more strain in the zone [36]. Both grain size refinement and work hardening in the NZ and TMAZ could contribute to the improvement of mechanical properties in such areas. This helps us to explain the reason for each area having different mechanical properties, as shown in Figure 5(b). For AA 6061, the high temperature during FSW destroys the original work hardened state in the NZ, TMAZ, and HAZ and leads the mechanical properties to weaken greatly. However, the grain size refinement and work hardening generated by stirring in the NZ and TMAZ improve the mechanical properties with some extent. As a result, the HAZ is the weakest area in FSW AA 6061. Since AA 5A06 is nonheat treatable, the high temperature during FSW does not affect the mechanical properties. With the strengthening of grain size refinement and work hardening, the hardness in the NZ and TMAZ of AA 5A06 becomes the strongest (Figure 5(b)).

3.5. Macro- and Microstructures of Fracture. Figures 8(a)–8(c) show the optical macrograph of the side view of fracture surface for samples 1, 2, and 3, and the fracture angle of the surface decreases from 35° to 10°. The decrease of the fracture angle

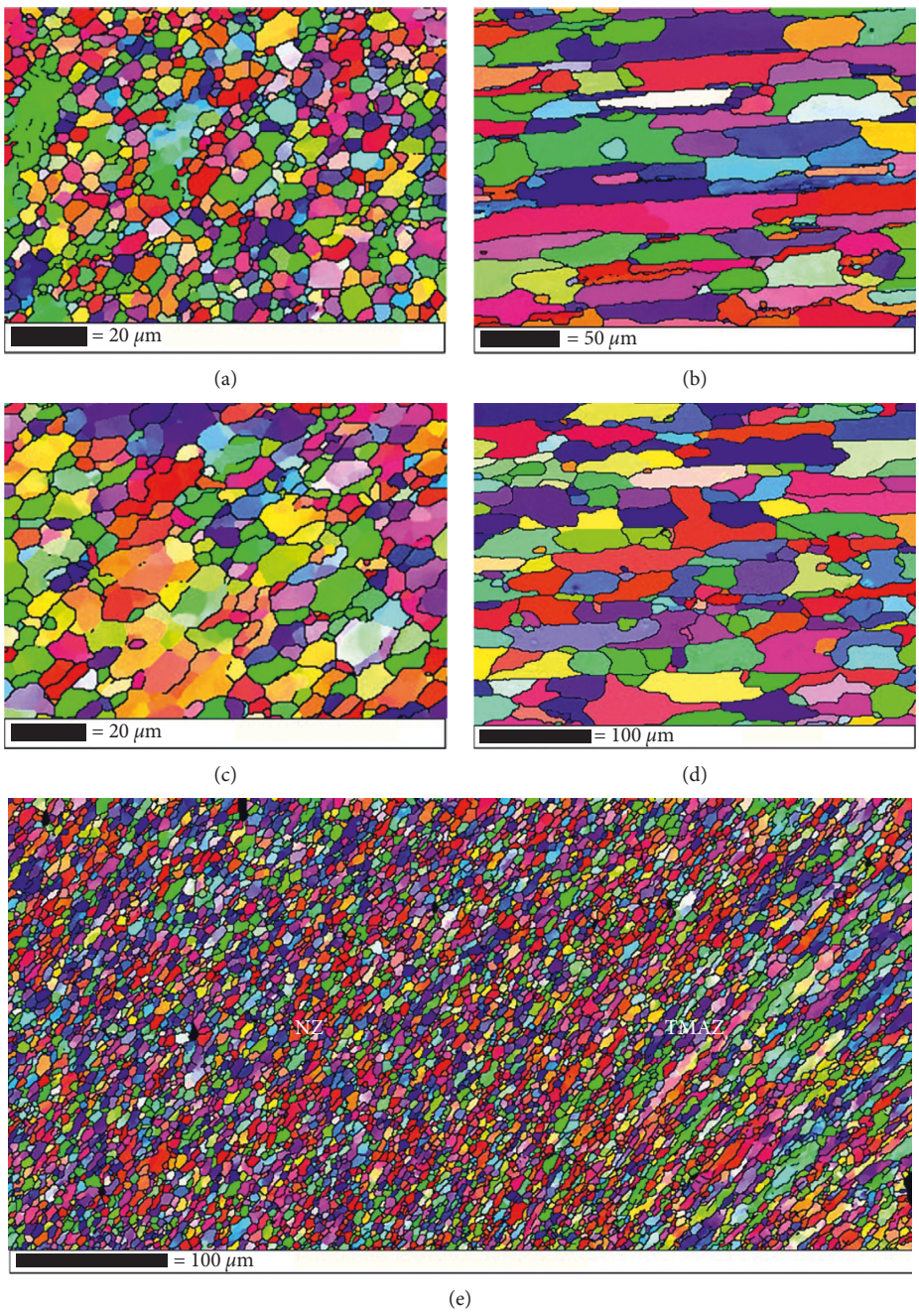

Figure 7: EBSD grain maps of FSW AA 6061-AA 5A06: (a) 5A06 NZ; (b) 5A06 BM; (c) 6061 NZ; (d) 6061 BM; (e) 6061 NZ-TMAZ.

could attribute to the change of the size and orientation of the HAZ. For samples 1, 2, and 3, the welding transverse speed was fixed at 150 mm/min and the rotation speeds were 600 rpm, 900 rpm, and 1200 rpm, respectively. With the increase of rotation speed, more heat was generated during FSW. The increasing heat input could enlarge the size of HAZ and change the orientation of HAZ. As discussed above, the HAZ of AA 6061 is the weakest area, and yielding firstly occurs in this region. Thus the initial yielding band shown in the DIC strain field could reflect the size and orientation of HAZ. From the strain field of samples 1, 2, and 3 at the beginning of yielding shown in Figures 8(a)–8(c), it could be found that the yielding band becomes thicker and the slant angle decreases gradually with increasing heat input. The change of size and orientation of HAZ was then intuitively revealed. The fracture angle agrees well with the slant angle of the HAZ. It could be concluded that the fracture angle of the welded specimen is determined by the size and orientation of the HAZ. Similar conclusion was obtained from Figures 8(d)–8(f) for samples 4, 5, and 6, where the rotation speed increases from 600 rpm to 1200 rpm with a fixed welding transverse speed of 100 mm/min.

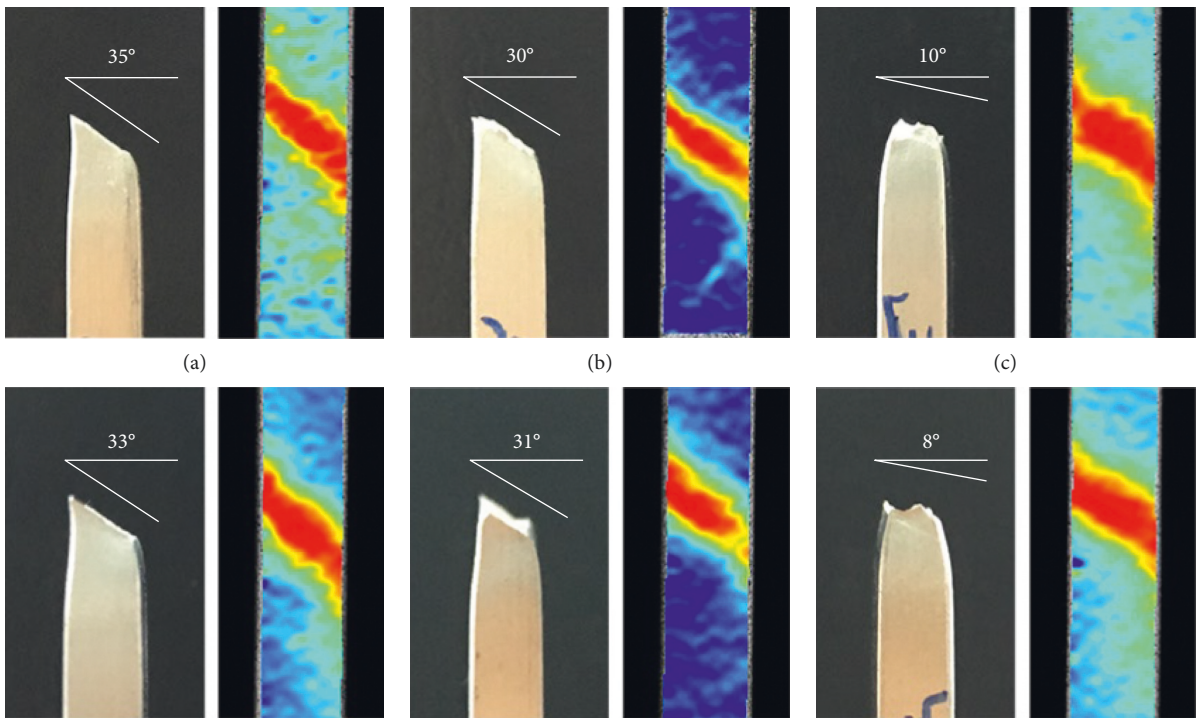

Figure 8: Optical macrograph of the side view of fracture surface and the corresponding strain field at the beginning of yielding for (a) Sample 1; (b) Sample 2; (c) Sample 3; (d) Sample 4; (e) Sample 5; (f) Sample 6.

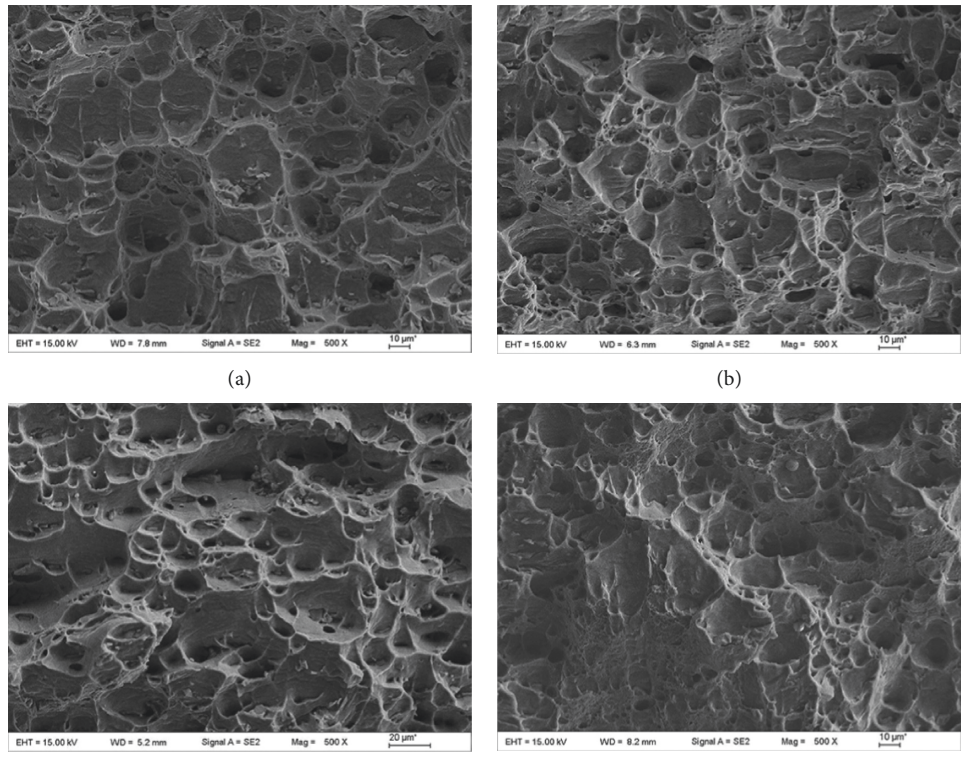

Figure 9: Continued.

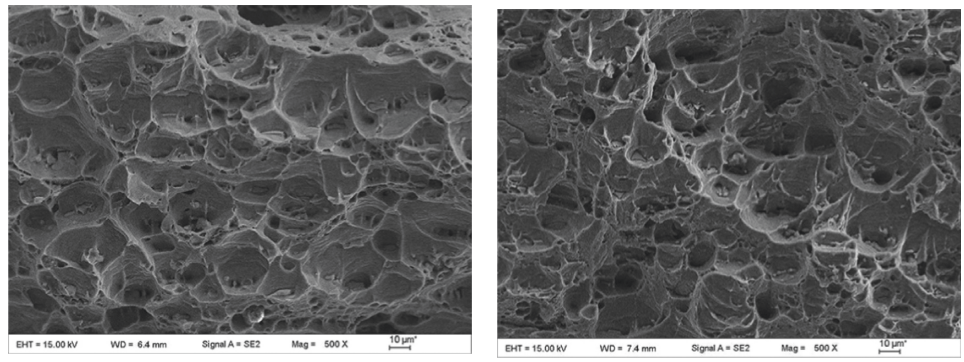

(e) (f)

Figure 9: SEM fractographs of FSW specimens: (a) Sample 1; (b) Sample 2; (c) Sample 3; (d) Sample 4; (e) Sample 5; (f) Sample 6.

From the SEM micrographs of the fracture surfaces shown in Figure 9, river patterns, cleavage steps, and tearing with small irregularly distributed dimples are observed. In Figures 9(a), 9(b), and 9(d)–9(f), most of the dimples are shallow and incline towards one direction. These characteristics are mainly caused by shear deformation. Due to the large fracture angle as shown in Figures 8(a), 8(b), and 8(d)–8(f), a large shear stress component exists along the fracture surface when the specimens are stretched. The shear stress could drive the materials to move relatively along the fracture surface to form shallow and inclined dimples. Thus, shear fracture should be the primary failure mode for samples 1, 2, 4, and 5. However, the equiaxed and normal dimples shown in Figures 8(c) and 8(f) indicate that the fracture of samples 3 and 6 is caused by normal stress. Since the macrofracture angles as shown in Figures 8(c) and 8(f) are small, the shear stress component along the fracture surface is ignorable, whilst the normal stress component is dominant. Under normal stress, the materials on both sides of the fracture surfaces eventually were pulled out from each other to form equiaxed and normal dimples.

4. Conclusions

In this paper, AA 6061 and AA 5A06 were successfully welded by FSW, and their microstructure and mechanical properties were analyzed. The grain structure evolution in stir zone is dominated by continuous dynamic recrystallization. The grain size refinement helps improve the mechanical properties in the HAZ and TMAZ of the weldments. Both the strain field evolution obtained by DIC and the nanoindentation hardness distribution map intuitively reveal that the welded HAZ of AA 6061 is the weakest region. Thus, the yielding, necking, and fracture occur in this zone. After welding, the yield strength of AA 6061 drops 50% to about 115 MPa and the ultimate tensile strength reduces from 277 MPa to about 190 MPa. Such a significant weakening of mechanical properties is mainly because the unstable work hardened state of rolled AA 6061 was destroyed by elevated temperature generated in FSW. The SEM analysis of fracture surface demonstrates that fractures in all tensile specimens are ductile fracture due to the presence of dimples. Furthermore, analyzing the micro- and macrofeatures of the fracture surfaces indicates that the increasing of heat input could enlarge the size of HAZ and reduce the slant angle of HAZ and thus leads the fracture angle to decrease and cause the dimples to change from inclined ones to normal ones. It was found that shear stress forms shallow and inclined dimples, whilst equiaxed and normal dimples are caused by normal stress.

Data Availability

The data used to support the findings of this study are available from the corresponding author upon request.

Conflicts of Interest

The authors declare that they have no conflicts of interest.

Acknowledgments

The authors would like to gratefully acknowledge the support from the National Natural Science Foundation of China (Grant Nos. 11727803, 11772302, 11672356, and 11402233) and Public Welfare Project of Zhejiang Province (2015C31074).

References

[1] T. Dursun and C. Soutis, "Recent developments in advanced aircraft aluminium alloys," *Materials & Design*, vol. 56, pp. 862–871, 2014.

[2] C. Menzemer and T. Srivatsan, "The effect of environment on fatigue crack growth behavior of aluminum alloy 5456," *Materials Science and Engineering: A*, vol. 271, no. 1-2, pp. 188–195, 1999.

[3] N. Guo, Y. Fu, Y. Wang, Q. Meng, and Y. Zhu, "Microstructure and mechanical properties in friction stir welded 5A06 aluminum alloy thick plate," *Materials & Design*, vol. 113, pp. 273–283, 2017.

[4] B. Gibson, D. Lammlein, T. Prater et al., "Friction stir welding: process, automation, and control," *Journal of Manufacturing Processes*, vol. 16, no. 1, pp. 56–73, 2014.

[5] M. Ericsson and R. Sandström, "Influence of welding speed on the fatigue of friction stir welds, and comparison with MIG and TIG," *International Journal of Fatigue*, vol. 25, no. 12, pp. 1379–1387, 2003.

[6] A. von Strombeck, G. Cam, J. F. dos Santos, V. Venzke, and M. Kocak, "A comparison between microstructure, properties, and toughness behavior of power beam and friction stir welds in Al-alloys," in *Proceedings of the TMS 2001 Annual Meeting Aluminum, Automotive and Joining*, pp. 12–14, New Orleans, LA, USA, February 2001.

[7] R. S. Mishra and Z. Ma, "Friction stir welding and processing," *Materials Science and Engineering: R: Reports*, vol. 50, no. 1-2, pp. 1–78, 2005.

[8] G. Çam and G. İpekoğlu, "Recent developments in joining of aluminum alloys," *International Journal of Advanced Manufacturing Technology*, vol. 91, no. 5–8, pp. 1851–1866, 2017.

[9] C. He, K. Kitamura, K. Yang, Y. J. Liu, Q. Y. Wang, and Q. Chen, "Very high cycle fatigue crack initiation mechanism in nugget zone of AA 7075 friction stir welded joint," *Advances in Materials Science and Engineering*, vol. 2017, Article ID 7189369, 10 pages, 2017.

[10] Z. Chen, S. Li, and L. H. Hihara, "Microstructure, mechanical properties and corrosion of friction stir welded 6061 aluminum alloy," 2015, http://arxiv.org/abs/1511.05507.

[11] Z. Chen, S. Li, K. Liu, and L. H. Hihara, "A study on the mechanical property and corrosion sensitivity of an AA5086 friction stir welded joint," 2015, http://arxiv.org/abs/1511.04990.

[12] J.-Q. Su, T. Nelson, R. Mishra, and M. Mahoney, "Microstructural investigation of friction stir welded 7050-T651 aluminium," *Acta Materialia*, vol. 51, no. 3, pp. 713–729, 2003.

[13] B. Yang, J. Yan, M. A. Sutton, and A. P. Reynolds, "Banded microstructure in AA2024-T351 and AA2524-T351 aluminum friction stir welds: part I," *Metallurgical Studies, Materials Science and Engineering: A*, vol. 364, no. 1-2, pp. 55–65, 2004.

[14] P. Cavaliere, R. Nobile, F. Panella, and A. Squillace, "Mechanical and microstructural behaviour of 2024–7075 aluminium alloy sheets joined by friction stir welding," *International Journal of Machine Tools and Manufacture*, vol. 46, no. 6, pp. 588–594, 2006.

[15] B. B. Wang, F. F. Chen, F. Liu, W. G. Wang, P. Xue, and Z. Y. Ma, "Enhanced mechanical properties of friction stir welded 5083Al-H19 joints with additional water cooling," *Journal of Materials Science & Technology*, vol. 33, no. 9, pp. 1009–1014, 2017.

[16] Y. Mao, L. Ke, Y. Chen, F. Liu, and L. Xing, "Inhomogeneity of microstructure and mechanical properties in the nugget of friction stir welded thick 7075 aluminum alloy joints," *Journal of Materials Science & Technology*, vol. 34, no. 1, pp. 228–236, 2018.

[17] Z. Chen, S. Li, and L. H. Hihara, "Electrochemical and mechanical behaviors of dissimilar friction stir welding between 5086 and 6061 aluminum alloy," 2018, http://arxiv.org/abs/1802.03460.

[18] M. Mahoney, C. Rhodes, J. Flintoff, W. Bingel, and R. Spurling, "Properties of friction-stir-welded 7075 T651 aluminum," *Metallurgical and Materials Transactions A*, vol. 29, no. 7, pp. 1955–1964, 1998.

[19] K. A. Hassan, A. Norman, D. Price, and P. Prangnell, "Stability of nugget zone grain structures in high strength Al-alloy friction stir welds during solution treatment," *Acta Materialia*, vol. 51, no. 7, pp. 1923–1936, 2003.

[20] G. Cam, G. Ipekoglu, and H. T. Serindag, "Effects of use of higher strength interlayer and external cooling on properties of friction stir welded AA6061-T6 joints," *Science and Technology of Welding and Joining*, vol. 19, no. 8, pp. 715–720, 2014.

[21] H. Jamshidi Aval, S. Serajzadeh, N. A. Sakharova, A. H. Kokabi, and A. Loureiro, "A study on microstructures and residual stress distributions in dissimilar friction-stir welding of AA5086–AA6061," *Journal of Materials Science*, vol. 47, no. 14, pp. 5428–5437, 2012.

[22] S. Mironov, T. Onuma, Y. S. Sato, and H. Kokawa, "Microstructure evolution during friction-stir welding of AZ31 magnesium alloy," *Acta Materialia*, vol. 100, pp. 301–312, 2015.

[23] J. C. V. Juarez, G. M. D. Almaraz, R. G. Hernandez, and J. J. V. Lopez, "Effect of modified pin profile and process parameters on the friction stir welding of aluminum alloy 6061-T6," *Advances in Materials Science and Engineering*, vol. 2016, Article ID 4567940, 9 pages, 2016.

[24] H. Zhang, M. Wang, W. Zhou et al., "Microstructure–property characteristics of a novel non-weld-thinning friction stir welding process of aluminum alloys," *Materials & Design*, vol. 86, pp. 379–387, 2015.

[25] H. Liu, Y. Zhao, Y. Hu, S. Chen, and Z. Lin, "Microstructural characteristics and mechanical properties of friction stir lap welding joint of alclad 7B04-T74 aluminum alloy," *International Journal of Advanced Manufacturing Technology*, vol. 78, no. 9–12, pp. 1415–1425, 2015.

[26] J.-R. Kim, E.-Y. Ahn, H. Das et al., "Effect of tool geometry and process parameters on mechanical properties of friction stir spot welded dissimilar aluminum alloys," *International Journal of Precision Engineering and Manufacturing*, vol. 18, no. 3, pp. 445–452, 2017.

[27] Y. Ma, J. H. Ye, G. J. Peng, D. H. Wen, and T. H. Zhang, "Nanoindentation study of size effect on shear transformation zone size in a Ni-Nb metallic glass," *Materials Science and Engineering: A*, vol. 627, pp. 153–160, 2015.

[28] Y. Ma, G. J. Peng, Y. H. Feng, and T. H. Zhang, "Nanoindentation investigation on the creep mechanism in metallic glassy films," *Materials Science and Engineering: A*, vol. 651, pp. 548–555, 2016.

[29] M. Peel, A. Steuwer, M. Preuss, and P. Withers, "Microstructure, mechanical properties and residual stresses as a function of welding speed in aluminium AA5083 friction stir welds," *Acta Materialia*, vol. 51, no. 16, pp. 4791–4801, 2003.

[30] K. Elangovan and V. Balasubramanian, "Influences of pin profile and rotational speed of the tool on the formation of friction stir processing zone in AA2219 aluminium alloy," *Materials Science and Engineering: A*, vol. 459, no. 1-2, pp. 7–18, 2007.

[31] M. A. Gharacheh, A. Kokabi, G. Daneshi, B. Shalchi, and R. Sarrafi, "The influence of the ratio of "rotational speed/traverse speed"(ω/v) on mechanical properties of AZ31 friction stir welds," *International Journal of Machine Tools and Manufacture*, vol. 46, no. 15, pp. 1983–1987, 2006.

[32] Z. Zhang, J. Bie, Y. Liu, and H. Zhang, "Effect of traverse/rotational speed on material deformations and temperature distributions in friction stir welding," *Journal of Materials Science & Technology*, vol. 24, no. 6, pp. 907–914, 2008.

[33] D. Wadeson, X. Zhou, G. Thompson, P. Skeldon, L. D. Oosterkamp, and G. Scamans, "Corrosion behaviour of friction stir welded AA7108 T79 aluminium alloy," *Corrosion Science*, vol. 48, no. 4, pp. 887–897, 2006.

[34] R. Kaibyshev, K. Shipilova, F. Musin, and Y. Motohashi, "Continuous dynamic recrystallization in an Al–Li–Mg–Sc alloy during equal-channel angular extrusion," *Materials*

Science and Engineering: A, vol. 396, no. 1-2, pp. 341–351, 2005.

[35] M. Rahmi and M. Abbasi, "Friction stir vibration welding process: modified version of friction stir welding process," *International Journal of Advanced Manufacturing Technology*, vol. 90, no. 1–4, pp. 141–151, 2017.

[36] O. Barooni, M. Abbasi, M. Givi, and B. Bagheri, "New method to improve the microstructure and mechanical properties of joint obtained using FSW," *International Journal of Advanced Manufacturing Technology*, vol. 93, no. 9–12, pp. 4371–4378, 2017.